JACS
JOURNAL OF THE AMERICAN CHEMICAL SOCIETY
Article
Cite This: J. Am. Chem. Soc. 2019, 141, 16884−16893
pubs.acs.org/JACS

Partial Oxidation-Induced Electrical Conductivity and Paramagnetism in a Ni(II) Tetraaza[14]annulene-Linked Metal Organic Framework

Yi Jiang,[†,⊥] Inseon Oh,[§,⊥] Se Hun Joo,[∥,⊥] Onur Buyukcakir,[†] Xiong Chen,[†] Sun Hwa Lee,[†] Ming Huang,[†] Won Kyung Seong,[†] Sang Kyu Kwak,*[,∥] Jung-Woo Yoo,*[,§] and Rodney S. Ruoff*[,†,‡,§,∥]

[†]Center for Multidimensional Carbon Materials (CMCM), Institute for Basic Science (IBS), Ulsan 44919, Republic of Korea
[‡]Department of Chemistry, Ulsan National Institute of Science and Technology (UNIST), Ulsan 44919, Republic of Korea
[§]School of Materials Science and Engineering, Ulsan National Institute of Science and Technology (UNIST), Ulsan 44919, Republic of Korea
[∥]School of Energy and Chemical Engineering, Ulsan National Institute of Science and Technology (UNIST), Ulsan 44919, Republic of Korea

Supporting Information

ABSTRACT: We report the synthesis and characterization of a two-dimensional (2D) conjugated Ni(II) tetraaza[14]annulene-linked metal organic framework (**NiTAA-MOF**) where **NiTAA** is a macrocyclic MN_4 (M = metal, N = nitrogen) compound. The structure of **NiTAA-MOF** was elucidated by Fourier-transform infrared, X-ray photoemission, and X-ray diffraction spectroscopies, in combination with density functional theory (DFT) calculations. When chemically oxidized by iodine, the insulating bulk **NiTAA-MOF** ($\sigma < 10^{-10}$ S/cm) exhibits an electrical conductivity of 0.01 S/cm at 300 K, demonstrating the vital role of ligand oxidation in the electrical conductivity of 2D MOFs. Magnetization measurements show that iodine-doped **NiTAA-MOF** is paramagnetic with weak antiferromagnetic coupling due to the presence of organic radicals of oxidized ligands and high-spin Ni(II) sites of the missing-linker defects. In addition to providing further insights into the origin of the induced electrical conductivity in 2D MOFs, both pristine and iodine-doped **NiTAA-MOF** synthesized in this work could find potential applications in areas such as catalase mimics, catalysis, energy storage, and dynamic nuclear polarization-nuclear magnetic resonance (DNP-NMR).

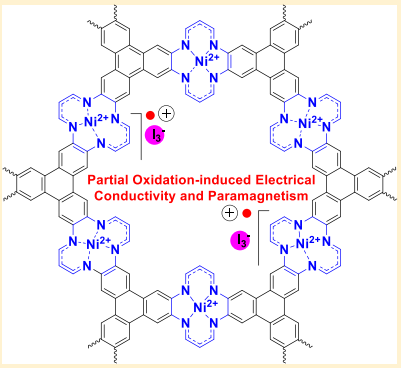

INTRODUCTION

Metal organic frameworks (MOFs) are coordination polymers in which metal ions/clusters are connected by organic ligands in a periodic manner.[1−6] In recent years, two-dimensional (2D) electrically conductive MOFs are being tested for applications in supercapacitors and resistive sensing.[7−10] Because of the large number of available organic building blocks and the possibility to combine them with different metal ions, 2D electrically conductive MOFs can be structurally diverse, and their chemical and physical properties can, in principle, be broadly tuned. Even so, the synthesis of electrically conducting 2D MOF materials has remained largely unexplored. To date, 2D conjugated MX_4-type (M = metal and X = NH, S, or O) MOFs with square-planar coordination of planar organic ligands (i.e., benzene, triphenylene, and coronene derivatives with thiol, hydroxyl, or amino groups) and metal atoms (i.e., Ni, Cu, Co, or Fe) have been investigated to obtain relatively high electrical conductivity.[11−21] It was found that the organic ligands in electrically conductive MX_4-type 2D MOFs were usually oxidized during synthesis to maintain charge neutrality with respect to the metal cation centers. Detailed understanding of the origin of electrical conductivity in MX_4-type MOFs is thus important for the future design of other electrically conducting MOFs but has not yet been achieved. In 2D MX_4-type MOFs, the extended $\pi-d$ conjugation was said to contribute significantly to their electrical conductivity,[13,21,22] although the authors of another paper reported that ligand oxidation in these materials is *likely* critical for increasing their electrical conductivity.[8] Partial oxidation/reduction of metals/ligands has been used to create other types of electrical conductive MOFs,[23,24] but here again, the role of ligand oxidation in the electrically conductivity of 2D MX_4-type MOFs is not clear, because the synthesis of crystalline unoxidized MX_4-type MOFs is challenging.[14]

Being synthetic analogues of naturally occurring porphyrins, tetraaza[14]annulenes are a class of well-known synthetic

Received: August 9, 2019
Published: October 14, 2019

DOI: 10.1021/jacs.9b08601
J. Am. Chem. Soc. 2019, 141, 16884−16893

Scheme 1. (a) Synthesis Route for the Model Compound NiTAA and (b) One-Step Formation of NiTAA-MOF under Solvothermal Conditions

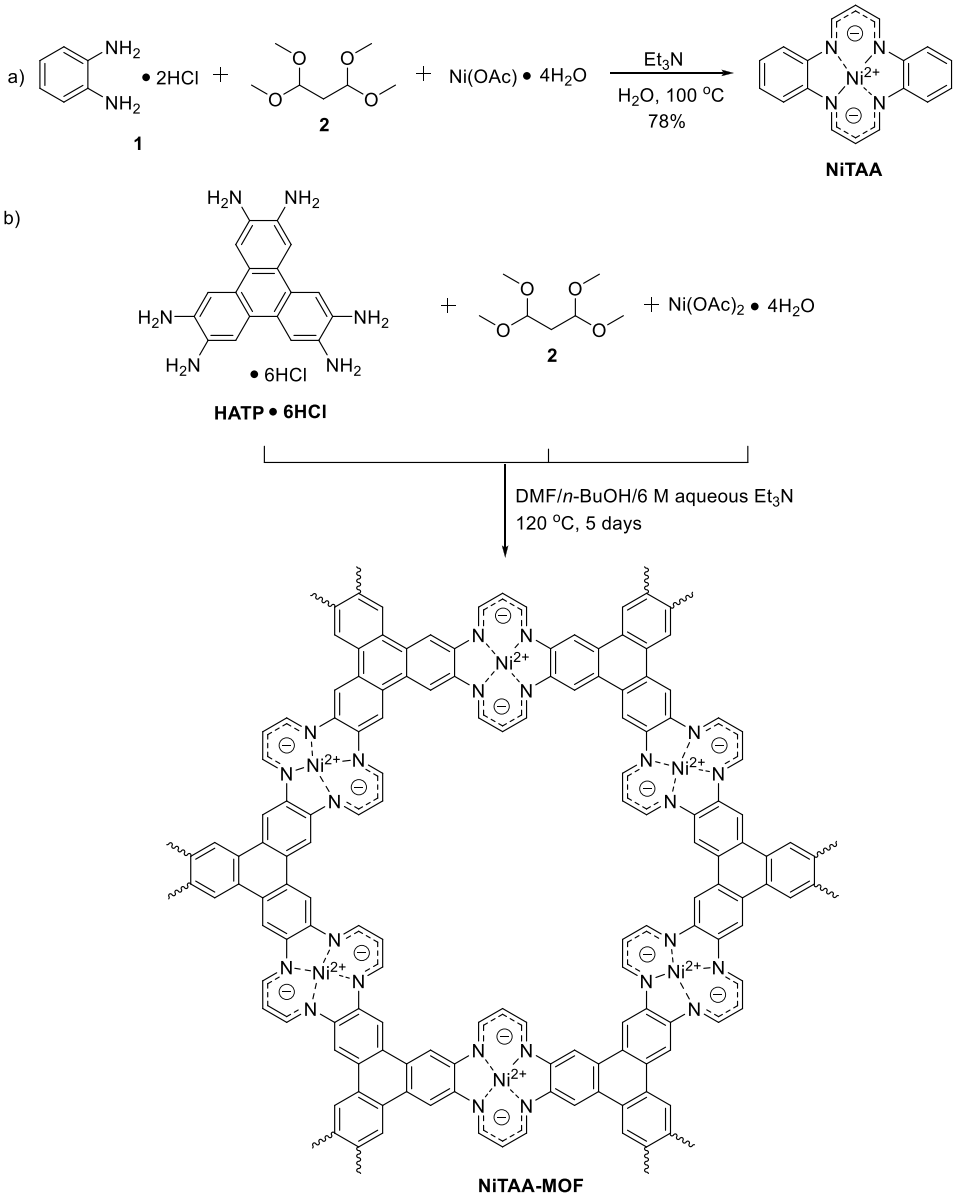

macrocycles.[25−28] The four nitrogen atoms of tetraaza[14]-annulenes can be easily deprotonated to generate dianionic ligands that coordinate with metal ions to form metal tetraaza[14]annulenes.[29,30] Metal tetraaza[14]annulenes have been applied in catalase mimics, field effect transistors, catalysts, and dye-sensitized solar cells.[31−34] Marks et al. reported that a partial oxidation of the ligand in Ni(II) tetraaza[14]annulene by iodine led to the formation of an electrically conductive metallo-macrocycle.[35] However, metal tetraaza[14]annulenes have not been used so far to produce framework materials, although attaching this macrocycle to a framework material could be promising for many applications. One characteristic difference between MN_4 [i.e., bis(*o*-diiminobenzosemiquinonato)metal(II) complex] and metal tetraaza[14]annulenes is that ligand oxidation in MN_4 usually occurs to achieve charge balance of metal cations,[34,36,37] whereas in tetraaza[14]annulenes, dianions are formed by deprotonation of nitrogen atoms to generate neutral metal tetraaza[14]annulenes by coordination with metal ions.[29,30] We reasoned that monitoring the change in electrical conductivity of metal tetraaza[14]annulene-linked MOFs before and after partial ligand oxidation could help to experimentally identify the role of ligand oxidation in inducing electrical conductivity in 2D MN_4-type MOFs. Moreover, it is also interesting to investigate the induced magnetism in this material due to such oxidized ligands, in view of its potential application as a polarizing agent in dynamic nuclear polarization-nuclear magnetic resonance (DNP-NMR) experiments. Here we report a porous 2D Ni tetraaza[14]annulene-linked MOF (**NiTAA-MOF**) synthesized by designing a cyclic Ni tetraaza[14]annulene formation reaction under an inert atmosphere (Scheme 1). Fourier-transform infrared (FT-IR), X-ray diffraction (XRD), and X-ray photoemission spectroscopy (XPS) were combined with density functional theory (DFT) calculations to establish the structure of **NiTAA-MOF**. A partially oxidized NiTAA-MOF sample was then produced

DOI: 10.1021/jacs.9b08601
J. Am. Chem. Soc. 2019, 141, 16884−16893

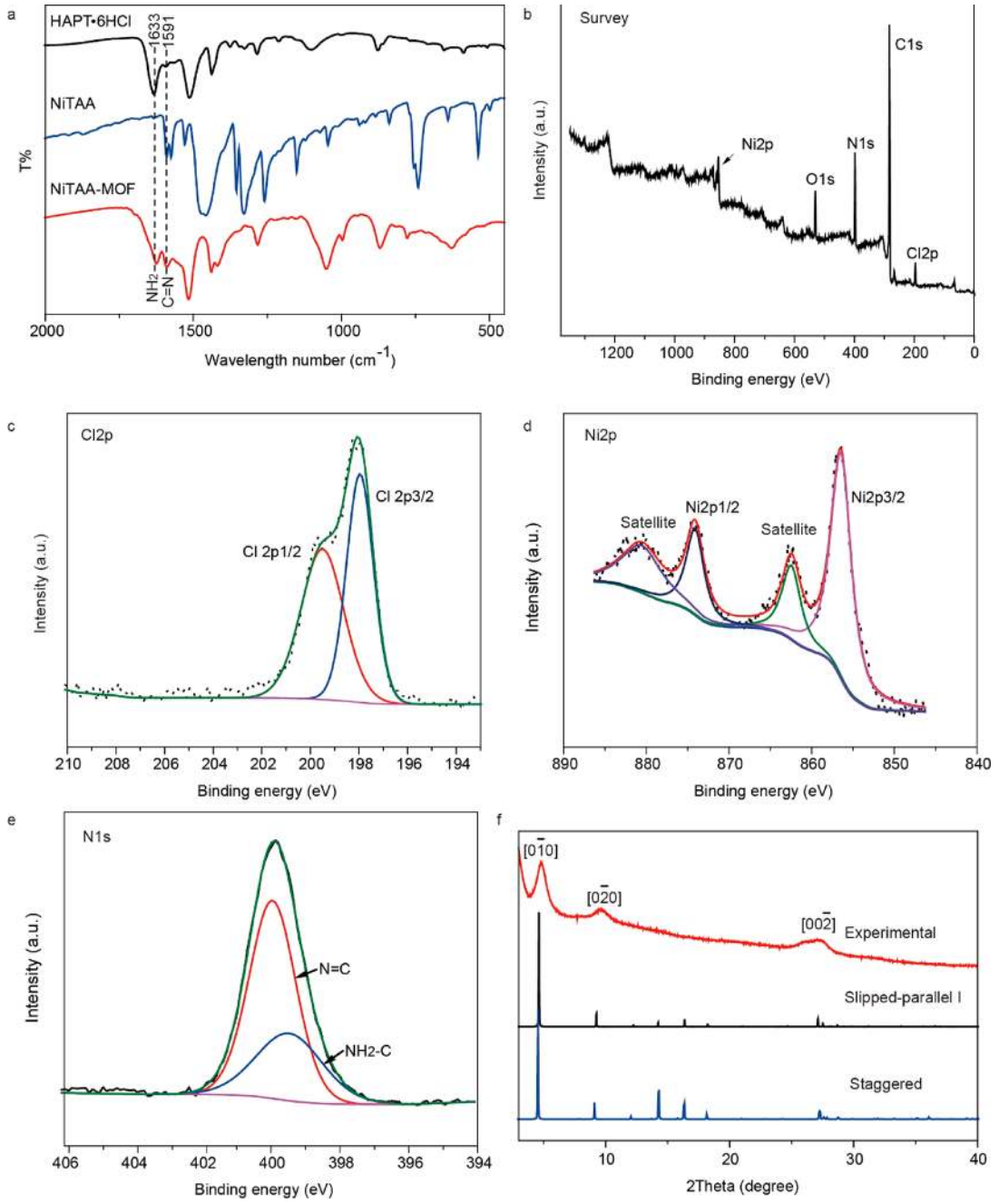

Figure 1. Structural characterization of **NiTAA-MOF**. (a) FT-IR spectra of HAPT·6HCl, the model compound **NiTAA**, and **NiTAA-MOF** powder. (b–e) Survey, high-resolution Cl 2p, Ni 2p, and N 1s XPS spectra of **NiTAA-MOF** powder, respectively. (f) XRD patterns of **NiTAA-MOF** powder: as obtained (red curve), and simulations using staggered (blue curve) and slipped-parallel (black curve) stacking I modes.

by iodine-doping; the oxidized material was characterized by XPS, Raman, and electron paramagnetic resonance (EPR). Electrical conductivity measurements on a bulk pellet obtained by pressing **NiTAA-MOF** powder at 1.2 GPa showed this material to be insulating ($\sigma < 10^{-10}$ S/cm), whereas the conductivity of an iodine-doped **NiTAA-MOF** pellet was ~0.01 S/cm, revealing the vital role of ligand oxidation in electrically conducting 2D MOFs. The iodine-doped **NiTAA-MOF** powder showed paramagnetic behavior with weak antiferromagnetic coupling originating both from the radicals of oxidized ligands and high-spin Ni(II) sites of missing-linker defects. Results from our work can be useful in the future design and realization of electrically conductive 2D MOFs; in addition, both pristine and iodine-doped **NiTAA-MOF** might be promising for applications in many areas including catalase mimics, catalysis, energy storage, and DNP-NMR.

RESULTS AND DISCUSSION

Synthesis and Structural Characterization of NiTAA-MOF. As shown in Scheme 1a, the reaction at 100 °C under an argon atmosphere of 1,2-phenylenediamine dihydrochloride (**1**) and 1,1,3,3-tetramethoxypropane (**2**) in the presence of triethylamine, with Ni(II) as a template, afforded the model compound **NiTAA** via the simultaneous formation of four imine bonds coordinated to Ni(II) atoms in 78% yield.[25,38] Note that the four-coordination mode without coordinated

DOI: 10.1021/jacs.9b08601
J. Am. Chem. Soc. 2019, 141, 16884–16893

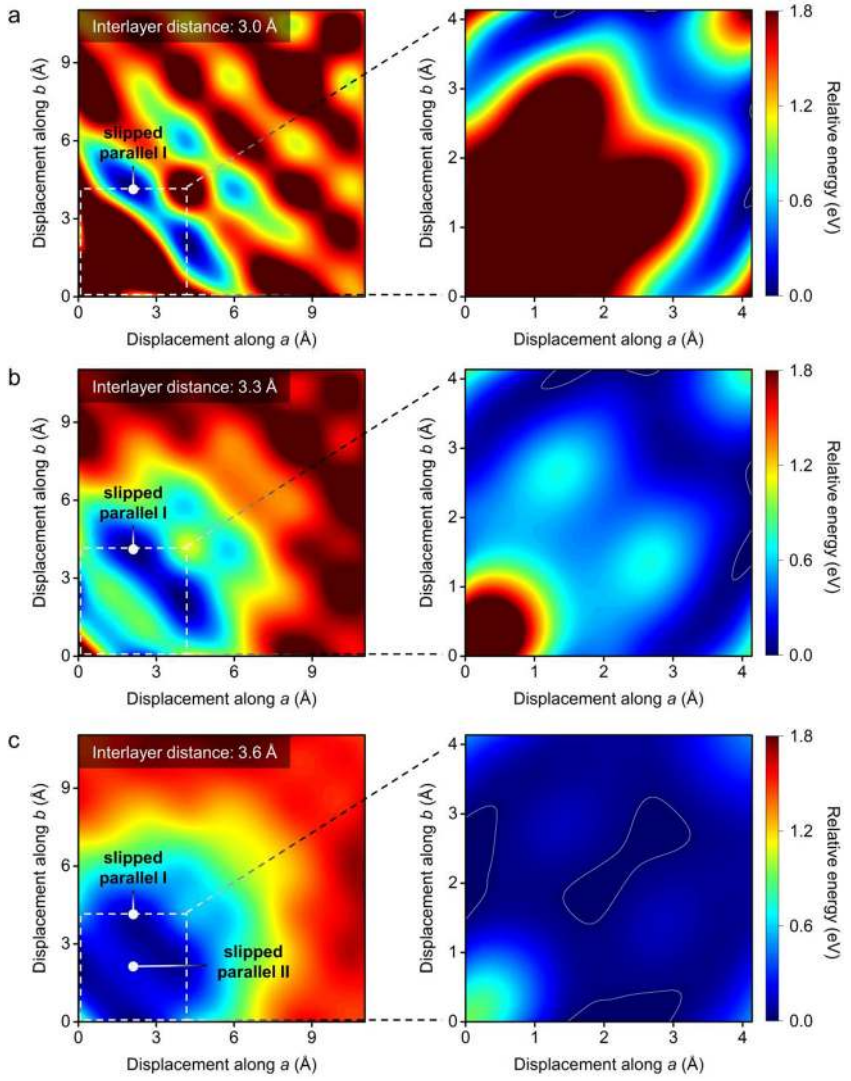

Figure 2. Potential energy surfaces (PESs) of **NiTAA-MOF** generated by interpolating DFT total energies for interlayer distances of (a) 3.0 Å, (b) 3.3 Å, and (c) 3.6 Å. White solid lines show the borders of the thermally accessible region.

solvent/counterions is typical for **NiTAA** derivatives.[26,29,39] Inspired by the successful synthesis of **NiTAA**, we reasoned that polycondensation of 1,2-phenylenediamine-based C_3-geometric monomers such as 2,3,6,7,10,11-hexaaminotriphenylene hexahydrochloride (HATP·6HCl), and the linear monomer **2**, with the Ni(II) atom as a template, might directly result in crystalline **NiTAA-MOF** through the simultaneous formation of multiple imine bonds (Scheme 1b). For the synthesis of **NiTAA-MOF**, a mixture of 2,3,6,7,10,11-hexaaminotriphenylene hexahydrochloride (HATP·6HCl), monomer **2** (1,1,3,3-tetramethoxypropane), and Ni(II) acetate tetrahydrate in a mixed solvent of DMF, *n*-BuOH, and 6 M aqueous triethylamine was maintained at 120 °C in a sealed ampule (that was degassed in advance) for 5 days. The **NiTAA-MOF** solid was collected by filtration; washed with water, THF, and methanol; and dried under an inert atmosphere. The formation of **NiTAA-MOF** was first evaluated by FT-IR spectroscopy. The FT-IR spectra of both **NiTAA** and **NiTAA-MOF** (Figure 1a) show a typical Ni(II) coordinated C═N peak at 1591 cm^{-1}, suggesting the formation of Ni(II) tetraaza[14]annulenes.[39] XPS was performed to determine the chemical composition of **NiTAA-MOF**. The survey spectrum of **NiTAA-MOF** (Figure 1b) reveals the presence of C, N, Ni, Cl, and O resonance signals; we attribute the O peak to moisture trapped in the pores of the framework and possible water molecules coordinated to the Ni(II) located at missing-linker defects (please see Scheme S1, SI). The high-resolution Cl 2p XPS spectrum (Figure 1c) shows two signals with binding energies of 199.5 and 198.0 eV, revealing the presence of unreacted intermediate species (missing-linker defects). Quantitative analysis of the Cl and Ni signals gives a Cl:Ni ratio of ~1.8:3.1, suggesting that ~71% of the Ni sites are linked by covalent bridges and ~29% have no covalent linkers. This result is consistent with elemental analysis data (Table S1, SI). In the high-resolution Ni 2p XPS spectrum (Figure 1d), two sets of peaks with binding energies of ~856.5 and ~874.2 eV were observed and assigned, respectively, to $2p_{3/2}$ and $2p_{1/2}$ levels of Ni. This result indicates that only Ni(II) is present in **NiTAA-MOF**, similar to the case of Ni(II) porphyrin.[40] The high-resolution N 1s XPS spectrum (Figure 1e) shows two peaks at 399.5 and 400.0 eV. The peak at 399.5 eV is assigned to unreacted nitrogen atoms (NH_2−C) of the missing-linker

DOI: 10.1021/jacs.9b08601
J. Am. Chem. Soc. 2019, 141, 16884−16893

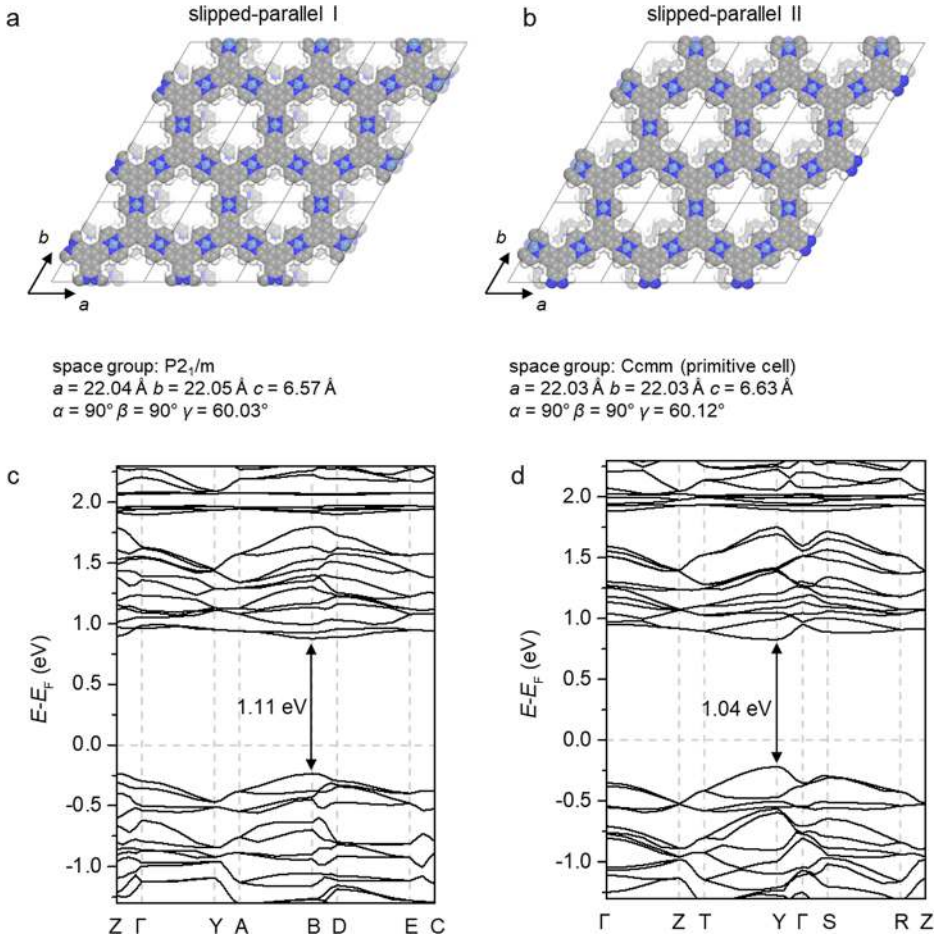

Figure 3. Space-filling models of **NiTAA-MOF** in (a) slipped-parallel I and (b) slipped-parallel II stacking modes, and (c, d) their corresponding calculated band structures. Carbon, hydrogen, nitrogen, and nickel atoms are gray, white, blue, and blue-gray, respectively.

defects, and that at 400.0 eV originates from imine nitrogen atoms bonded to Ni atoms.[41]

The X-ray diffraction (XRD) pattern of bulk **NiTAA-MOF** powder (Figure 1f, red curve) shows peaks at 4.8° and 9.6°, which can be assigned, respectively, to reflections from $(0\bar{1}0)$ and $(0\bar{2}0)$ planes in the proposed structure. This result is indicative of the good long-range order within the *ab*-plane. An additional peak due to the $(00\bar{2})$ plane was observed at 27.3°, suggesting structural ordering with a 3.27 Å separation perpendicular to the 2D sheets. Density functional theory (DFT) calculations were performed to obtain the optimum monolayer **NiTAA-MOF** structure and ascertain its packing mode (see computational details in SI). The potential energy surfaces (PESs, Figure 2) were thus generated using several different interlayer distances while introducing different translations (*ab*-plane displacements) between the top and bottom layers. Using this approach, the change in PESs can be explored with respect to the displacement of the **NiTAA-MOF** sheets (along *a* or *b*), as well as the interlayer distance. We chose three different interlayer distances of 3.6, 3.3, and 3.0 Å, which are, respectively, the interlayer distance of **NiTAA-MOF** with the eclipsed stacking mode, the value observed in the experiment, and a distance which is smaller than the experimental value. To sample the PESs, all single point DFT energies were calculated using VASP software while implementing Grimme's D3 method.

Figure 2 shows the PESs generated at the interlayer distances of 3.0, 3.3, and 3.6 Å. At the interlayer distances of 3.0 and 3.3 Å, the slipped-parallel I stacking mode, in which the **NiTAA-MOF** sheet is shifted by 1/16 of a cell edge along the *a*-direction and 3/16 of a cell edge along the *b*-direction, is the most stable (Figure 2a,b). At the interlayer distance of 3.6 Å, the slipped-parallel II stacking mode, in which there is a shift of ∼2/16 of a cell edge along both *a*- and *b*-directions, is the most stable (Figure 2c). Thus, the slipped-parallel I stacking mode becomes a local minimum structure, even with a relatively high energy of 0.078 eV, when compared to the slipped-parallel II stacking mode. The interlayer distance dependence of these two minimum energy structures can be seen in Figure S4, which shows the total system energies for the two stacking modes at the three interlayer distances of 3.0, 3.3, and 3.6 Å. Both structures have the lowest energy at the interlayer distance of 3.3 Å. In particular, we note that the slipped-parallel I stacking mode is the most stable. Considering the range of the interlayer distances observed experimentally, we suggest that the slipped-parallel I stacking mode is the overall minimum energy structure.

In addition, geometry optimizations of the two minimum energy structures (i.e., slipped-parallel I and II stacking modes, Figure 3a,b) were also performed. The interlayer distance of the optimized structure for both stacking modes is ∼3.3 Å, which agrees well with the experimental value. More importantly, the slipped-parallel I stacking mode, even after

DOI: 10.1021/jacs.9b08601
J. Am. Chem. Soc. 2019, 141, 16884−16893

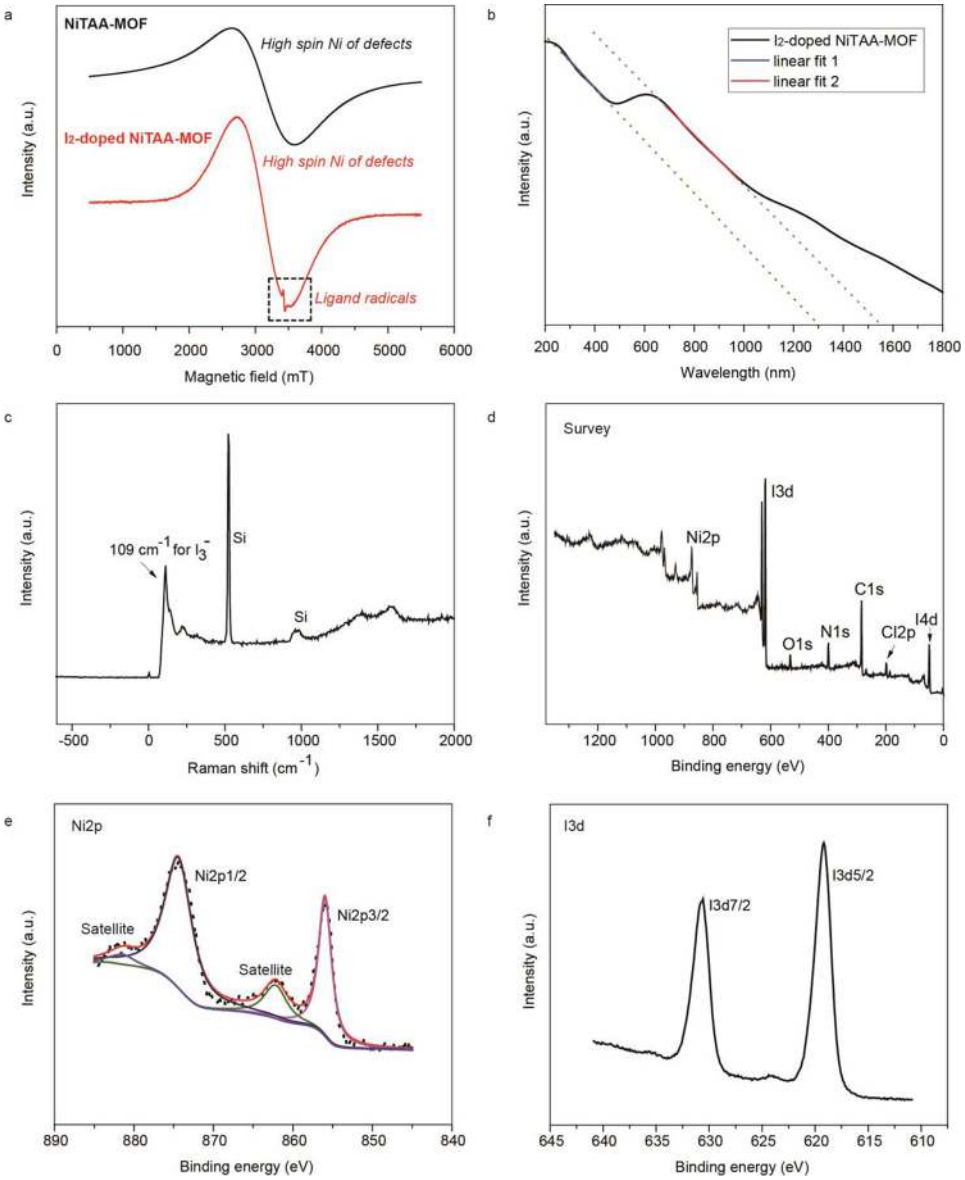

Figure 4. Structure characterization of iodine-doped **NiTAA-MOF**. (a) EPR spectra of pristine and iodine-doped **NiTAA-MOF**. (b) Diffuse reflectance UV−vis spectrum of iodine-doped **NiTAA-MOF**. (c) Raman spectrum of iodine-doped **NiTAA-MOF** on Si/SiO_2 substrate. (d−f) Survey, high-resolution Ni 2p and I 3d XPS spectra, respectively, of iodine-doped **NiTAA-MOF**.

geometry optimization, has a lower energy when compared to the slipped-parallel II stacking mode, which is consistent with PES results. The simulated XRD pattern of **NiTAA-MOF** with the slipped-parallel I stacking mode matches well with the experimental result (Figure 1f). The above results thus indicate that the **NiTAA-MOF** structure with the slipped-parallel I stacking mode can be considered to be the global minimum energy structure. The band structures of these two slipped plane structures were calculated as shown in Figure 3c,d. Both structures have a direct band gap, and the band gap values are close to each other (1.11 eV at the B point for the slipped-parallel I stacking mode, and 1.04 eV at the Y point for the slipped-parallel II stacking mode). This result indicates that the type of slipped-parallel stacking mode does not affect the electronic properties of **NiTAA-MOF**.

To further evaluate the structure of 2D **NiTAA-MOF**, high-resolution transmission electron microscopy (HR-TEM) of the as-synthesized **NiTAA-MOF** was done. The HR-TEM image of **NiTAA-MOF** (Figure S5) shows parallel lines with a repeat distance of ∼1.9 nm, which are assigned to the $(0\bar{1}0)$ planes. Nitrogen sorption isotherms of bulk **NiTAA-MOF** powder were recorded at 77 K to determine its porosity (Figure S7). The Brunauer−Emmett−Teller (BET) surface area and the total pore volume were calculated to be 47 $m^2\ g^{-1}$ and 0.075 $cm^3\ g^{-1}$, respectively. The pore size distribution profile (Figure S7b) shows a large number of micropores with entrance diameter ∼1.16 nm, which is in agreement with the simulated pore size of ∼1.2 nm from the slipped-parallel I packing mode; this further supports the assigned structure of the 2D **NiTAA-MOF**.

Electrical Conductivity of Iodine-Doped NiTAA-MOF. Electrical conductivity measurements using the four-point-probe method showed that the bulk compressed pristine **NiTAA-MOF** pellet was insulating ($\sigma < 10^{-10}$ S/cm), even though (nominally) having an an extended 2D π−d conjugated structure. Inspired by previous reports that the electrical

DOI: 10.1021/jacs.9b08601
J. Am. Chem. Soc. 2019, 141, 16884−16893

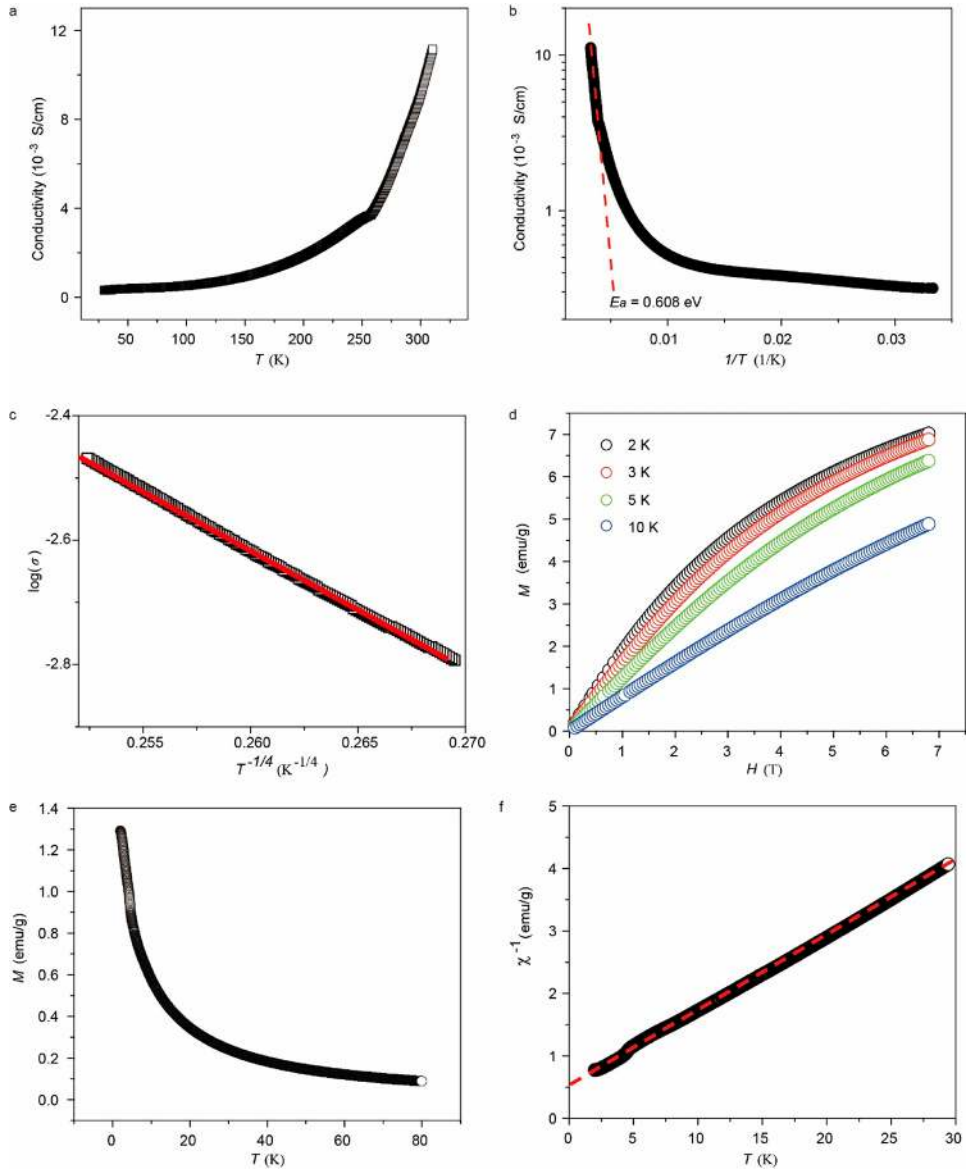

Figure 5. Electrical conductivity and magnetic properties of iodine-doped **NiTAA-MOF**. (a) Electrical conductivity as a function of temperature from 5 to 310 K. (b) Plot of electrical conductivity (σ) versus $1/T$. (c) $\log(\sigma)$ versus $T^{-1/4}$ plot in the temperature range from 180 to 250 K. (d) Field-dependent magnetization of **NiTAA-MOF** measured at various temperatures. (e) Temperature dependence of magnetization obtained under an applied field of H = 1000 Oe. (f) Plot of χ^{-1} versus T.

conductivity of **NiTAA** can be triggered by partial ligand oxidation through iodine-doping,[35,42,43] we investigated the effect of ligand oxidation on the electrical conductivity of **NiTAA-MOF**. Iodine-doping was carried out by heating the sample under I_2 vapor in a sealed container at 80 °C for 12 h. The EPR spectrum of the as-synthesized **NiTAA-MOF** (Figure 4a) shows only a broad signal with a g value of 2.209, which can be assigned to high-spin Ni(II) ions of missing-linker defects.[44,45] In contrast to that of pristine **NiTAA-MOF**, an additional EPR signal with a g value of 2.005 was observed for the iodine-doped **NiTAA-MOF**, indicating the formation of organic radicals due to ligand oxidation (Figure 4a). The diffuse reflectance UV−vis spectrum of the iodine-doped **NiTAA-MOF** shows a broad absorption band extending up into the near-infrared region (Figure 4b), and two band gaps at the wavelengths of 1301 nm (0.96 eV) and 1549 nm (0.80 eV) were observed. Raman spectroscopy was performed to determine the nature of the iodine species in iodine-doped **NiTAA-MOF**. In the Raman spectrum of iodine-doped **NiTAA-MOF** (Figure 4c), two signals at 109 and 216 cm^{-1} were observed, both of which were characteristic of symmetrical I_3^- ions and precluded the presence of I_2 and I_5^- species.[46] The survey XPS spectrum of the iodine-doped **NiTAA-MOF** (Figure 4d) shows the presence of C, N, Ni, Cl, O, and I resonance signals. In the high-resolution Ni 2p XPS spectrum (Figure 4e), the two peaks located at 860.0 and 874.3 eV are assigned, respectively, to the $2p_{1/2}$ and $2p_{3/2}$ core levels of Ni(II), indicating that oxidation occurred on the organic ligands of **NiTAA** units rather than on Ni(II) ions.[42] The high-resolution I 3d XPS spectrum (Figure 4f) shows two signals at 630.7 and 619.1 eV, which correspond to I $3d_{7/2}$ and $3d_{5/2}$ levels, also confirming the presence of I_3^- anions after iodine-doping. Quantitative analysis of the Ni and I signals gives a Ni:I ratio of ∼1:0.4, suggesting that a partial oxidation (∼13%) was induced by iodine-doping.

DOI: 10.1021/jacs.9b08601
J. Am. Chem. Soc. 2019, 141, 16884−16893

The electrical conductivity of bulk iodine-doped **NiTAA-MOF** was measured by using 4-probe methods with a Keithley 2636A sourcemeter and a 2182 nanovoltmeter. The pelletized sample with a thickness of 0.12 mm was prepared by pressing the powder at 1.2 GPa. Bulk iodine-doped **NiTAA-MOF** showed an electrical conductivity of ~0.01 S/cm at 300 K (Figure 5a). This value is in line with those reported for an iron-quinoid MOF[23] and $K_xFe_2(BDP)_3$ (BDP^{2-} = 1,4-benzenedipyrazolate),[24] and higher than those measured for cobalt 2,3,6,7,10,11-triphenylenehexathiolate and $[Cu_3(C_6O_6)_2]$ MOFs.[12,22] Similar to the electrically conductive MOFs produced through chemical reduction reported in the literature,[24] the relatively high electrical conductivity of the iodine-doped **NiTAA-MOF** is due to the formation of free carriers by the partial ligand oxidation and the extensive electron delocalization in the well-defined layer structure. Due to the probably anisotropic nature of the conductivity in nanocrystalline samples and due to interparticle resistance, the measured conductivity of pressed pellets could be considerably lower than the true conductivity of this 2D material, and this aspect should be further investigated by making measurements on larger crystallites or continuous thin films.[47] The observed electrical conductivity of the iodine-doped **NiTAA-MOF** (0.01 S/cm) is, however, lower than that obtained for a $Ni_3(HITP)_2$ framework (2 S/cm)[21] due to the lower degree of ligand oxidation. The temperature-dependent conductivity profile (Figure 5a) measured using a four-probe method shows an exponential increase with temperature, indicating the semiconducting nature of the pellet sample.[13,17] Figure 5b displays the plot of electrical conductivity (σ) as a function of the reciprocal of temperature ($1/T$). A linear region is observed over the temperature range 260–310 K, indicating that thermally activated transport is dominant in this temperature range. The slope of the linear region near room temperature corresponds to E_a/k_B, where E_a is the activation energy, and k_B is the Boltzmann constant (8.617×10^{-5} eV/K). The value of E_a calculated using the Arrhenius law was found to be ~0.608 eV.[8,15] Note that E_a represents the energy barrier that carriers must overcome when they hop between sites, which is different from the typical semiconducting band gap energy between valence and conduction bands in the individual crystallite. The temperature-dependent conductivity below around 150 K (note that the electrical conductivity at 30 K is 3.2×10^{-4} S/cm) only weakly depends on temperature, indicating that charge hopping in this regime takes place largely through tunneling. In addition, a plot of log (σ) versus $T^{-1/4}$ over the temperature range 180–250 K (Figure 5c) is linear, in agreement with the 3D Mott variable range hopping (Mott-VRH) mechanism.[48] The overall behavior of the temperature-dependent conductivity implies that the charge transport in bulk polycrystalline pellets is dominated by hopping over grain boundaries between the crystallites, resulting in a semiconductor-like behavior,[49] which means that the individual 2D MOF is conductive and could be a metal or a semiconductor. We note that several earlier reports attributed such a T dependence to the semiconducting property of the polymer itself.[21,22] However, from this result alone, we can only infer that the individual 2D MOF is either semiconducting or metallic, and not a wide band gap insulator.

Paramagnetism of Iodine-Doped NiTAA-MOF. The magnetic properties of the iodine-doped **NiTAA-MOF** powder were probed using superconducting quantum interference device (SQUID) magnetometry. Figure 5d shows magnetization as a function of the applied magnetic field measured at various temperatures. The magnetization at 2 K shows a substantial increase and saturates at high magnetic fields, indicating a typical paramagnetic behavior. To further explore the magnetic characteristics of the iodine-doped **NiTAA-MOF**, we measured the temperature dependence of magnetization as shown in Figure 5e. Magnetization increased steeply with decreasing temperature, which is typical of paramagnetic materials. The paramagnetic spins of the iodine-doped **NiTAA-MOF** are associated with radicals of the oxidized ligands[43] and high-spin Ni(II) sites located at the missing-linker defects,[44,45] as verified by EPR (Figure 4a). The χ^{-1} versus T plot displays a straight line (Figure 5f) following Curie's law. In particular, the χ^{-1} versus T curve shows a negative intercept with a Weiss temperature of ~−3 K, indicating the presence of weak antiferromagnetic coupling. We note that the structure of the iodine-doped **NiTAA-MOF** forms a Kagome lattice, which means that, at very low temperatures, antiferromagnetic coupling between nearest neighbor spins will eventually lead to a spin glass phase due to frustration.[50,51]

CONCLUSIONS

We have synthesized a 2D π–d conjugated **NiTAA-MOF** and characterized its structure using XPS, FT-IR, and PXRD combined with DFT calculations. Results show slipped-parallel packing between neighboring layers with a calculated direct band gap of 1.11 eV for the material. A compressed as-synthesized **NiTAA-MOF** pellet was found to be insulating ($\sigma < 10^{-10}$ S/cm), whereas a bulk compressed iodine-doped **NiTAA-MOF** pellet had a relatively high electrical conductivity of 0.01 S/cm at 300 K, revealing the vital role of ligand oxidation in the electrical conductivity of 2D MOFs. Magnetic analysis showed that iodine-doped **NiTAA-MOF** is paramagnetic with weak antiferromagnetic coupling due to both radicals of oxidized ligands and the high-spin Ni(II) of missing-linker defects. The insights gained in this study can help in the future design and realization of electrically conductive MOFs. We also suggest that the as-synthesized and iodine-doped **NiTAA-MOFs** might be applicable in areas including catalase mimics, catalysis, and energy storage.

EXPERIMENTAL SECTION

Methods. FT-IR was performed with an Agilent 600 Series FT-IR spectrometer. XPS data were collected using an ESCALAB 250Xi XPS, and TGA (TA Instrument Q 500 analyzer) was conducted under N_2 by heating to 900 °C at the rate of 5 °C min^{-1}. Nitrogen sorption analysis was carried out using a surface area and porosity analyzer (Micromeritics ASAP2020); the samples were degassed under vacuum at 100 °C for 10 h before sorption measurements. XRD was performed on a Rigaku SmartLab powder X-ray diffractometer, and magnetic properties were measured using a SQUID magnetometer (Quantum Design SQUID-VSM). Electrical properties were measured in a PPMS (Quantum Design physical property measurements system) with the help of an external electrometer (Keithley 2636A and 2182) with high impedance. A pressed pellet (5×8 mm^2 size and 0.12 mm thickness) was prepared for electrical measurement. Four-terminal Ti (5 nm)/Au (100 nm) contacts with 1 mm separations were deposited by thermal evaporation. Electrical contacts to the Au pads were made using Ag paste to copper wires. Raman spectroscopy (Wi-Tec micro Raman) was done under 532 nm laser excitation under ambient conditions. TEM was carried out on a Jeol JEM-2100F TEM instrument. The freeze-drying was performed in a freeze-dryer (SCANVAC CoolSafe, LABOGENE).

DOI: 10.1021/jacs.9b08601
J. Am. Chem. Soc. 2019, 141, 16884–16893

Synthesis of NiTAA-MOF. 1,1,3,3-Tetramethoxypropane (69 μL, 0.42 mmol), Ni(II) acetate tetrahydrate (52.4 mg, 0.21 mmol), and 2,3,6,7,10,11-hexaaminotriphenylene hexahydrochloride (HATP·6HCl, 75 mg, 0.14 mmol)[52] were added to a *n*-BuOH/DMF solvent mixture (7.5 mL, 1/2 v/v) contained in a Pyrex tube. After the addition of 6 M aqueous Et_3N (0.14 mL, 0.84 mmol), the mixture was sonicated to form a homogeneous dispersion, which was degassed by three freeze–pump–thaw cycles. The tube was flame-sealed and heated at 120 °C for 5 days. The solid was collected by filtration and washed with water, THF, and methanol under an inert atmosphere. The obtained solid (yield: 83%) was finally dried under high vacuum (10^{-3} Torr) and stored in a glovebox. The chemical stability of **NiTAA-MOF** was tested by XRD after treating it for 7 days in boiling water and 9 M NaOH (aq), and 1 day in 1 M HCl (aq) under Ar (Figure S10a). It was found that **NiTAA-MOF** retained its good crystallinity after treatment in boiling water or 9 M NaOH (aq), whereas it became amorphous in 1 M HCl (aq).

Synthesis of Iodine-Doped NiTAA-MOF. The pristine **NiTAA-MOF** powder was charged in a sealed container and heated with I_2 vapor at 80 °C followed by repeated washing with several portions of *n*-hexane, drying for 8 h under vacuum (10^{-3} Torr), and freeze-drying for 12 h under 0.1 Pa pressure at −108 °C, to prepare iodine-doped **NiTAA-MOF**.

■ ASSOCIATED CONTENT

Supporting Information

The Supporting Information is available free of charge on the ACS Publications website at DOI: 10.1021/jacs.9b08601.

Synthesis and characterization of the model compound **NiTAA**, computational details, TGA, additional XPS spectra, results from DFT calculations, ICP-mass spectroscopic analysis, and elemental analysis (PDF)

■ AUTHOR INFORMATION

Corresponding Authors

*skkwak@unist.ac.kr
*jwyoo@unist.ac.kr
*rsruoff@ibs.re.kr, ruofflab@gmail.com

ORCID

Yi Jiang: 0000-0003-1080-5884
Se Hun Joo: 0000-0003-4507-150X
Onur Buyukcakir: 0000-0003-4626-8232
Ming Huang: 0000-0002-9188-4619
Sang Kyu Kwak: 0000-0002-0332-1534
Jung-Woo Yoo: 0000-0001-7038-4001

Author Contributions

⊥Y.J., I.O., and S.H.J. contributed equally to this work.

Notes

The authors declare no competing financial interest.

■ ACKNOWLEDGMENTS

This work was supported by IBS-R019-D1, the National Research Foundation of Korea (NRF) grant funded by the Korean government (2017M3A7B4049172 and 2017R1A2B4008286), and the Outstanding Research Fund (1.180066.01) of UNIST (Ulsan National Institute of Science & Technology). Computational resources used in this work were from CMCM and UNIST-HPC.

■ REFERENCES

(1) Furukawa, H.; Cordova, K. E.; O'Keeffe, M.; Yaghi, O. M. The Chemistry and Applications of Metal-Organic Frameworks. *Science* **2013**, *341*, 1230444.

(2) Ferey, G. Hybrid Porous Solids: Past, Present, Future. *Chem. Soc. Rev.* **2008**, *37*, 191–214.

(3) Li, J. R.; Sculley, J.; Zhou, H. C. Metal-Organic Frameworks for Separations. *Chem. Rev.* **2012**, *112*, 869–932.

(4) Yaghi, O. M.; O'Keeffe, M.; Ockwig, N. W.; Chae, H. K.; Eddaoudi, M.; Kim, J. Reticular Synthesis and the Design of New Materials. *Nature* **2003**, *423*, 705–714.

(5) Zhou, H. C.; Long, J. R.; Yaghi, O. M. Introduction to Metal-Organic Frameworks. *Chem. Rev.* **2012**, *112*, 673–674.

(6) Zhu, Q. L.; Xu, Q. Metal-Organic Framework Composites. *Chem. Soc. Rev.* **2014**, *43*, 5468–5512.

(7) Hendon, C. H.; Tiana, D.; Walsh, A. Conductive Metal-Organic Frameworks and Networks: Fact or Fantasy? *Phys. Chem. Chem. Phys.* **2012**, *14*, 13120–13132.

(8) Sun, L.; Campbell, M. G.; Dincă, M. Electrically Conductive Porous Metal-Organic Frameworks. *Angew. Chem., Int. Ed.* **2016**, *55*, 3566–3579.

(9) Talin, A. A.; Centrone, A.; Ford, A. C.; Foster, M. E.; Stavila, V.; Haney, P.; Kinney, R. A.; Szalai, V.; El Gabaly, F.; Yoon, H. P.; Leonard, F.; Allendorf, M. D. Tunable Electrical Conductivity in Metal-Organic Framework Thin-Film Devices. *Science* **2014**, *343*, 66–69.

(10) Wang, H.; Zhu, Q.-L.; Zou, R.; Xu, Q. Metal-Organic Frameworks for Energy Applications. *Chem.* **2017**, *2*, 52–80.

(11) Campbell, M. G.; Sheberla, D.; Liu, S. F.; Swager, T. M.; Dinca, M. Cu_3(hexaiminotriphenylene)$_2$: An Electrically Conductive 2D Metal-Organic Framework for Chemiresistive Sensing. *Angew. Chem., Int. Ed.* **2015**, *54*, 4349–4352.

(12) Clough, A. J.; Skelton, J. M.; Downes, C. A.; de la Rosa, A. A.; Yoo, J. W.; Walsh, A.; Melot, B. C.; Marinescu, S. C. Metallic Conductivity in a Two-Dimensional Cobalt Dithiolene Metal-Organic Framework. *J. Am. Chem. Soc.* **2017**, *139*, 10863–10867.

(13) Dong, R.; Zhang, Z.; Tranca, D. C.; Zhou, S.; Wang, M.; Adler, P.; Liao, Z.; Liu, F.; Sun, Y.; Shi, W.; Zhang, Z.; Zschech, E.; Mannsfeld, S. C. B.; Felser, C.; Feng, X. A Coronene-Based Semiconducting Two-Dimensional Metal-Organic Framework with Ferromagnetic Behavior. *Nat. Commun.* **2018**, *9*, 2637.

(14) Feng, D.; Lei, T.; Lukatskaya, M. R.; Park, J.; Huang, Z.; Lee, M.; Shaw, L.; Chen, S.; Yakovenko, A. A.; Kulkarni, A.; Xiao, J.; Fredrickson, K.; Tok, J. B.; Zou, X.; Cui, Y.; Bao, Z. Robust and Conductive Two-Dimensional Metal-Organic Frameworks with Exceptionally High Volumetric and Areal Capacitance. *Nat. Energy* **2018**, *3*, 30–36.

(15) Hmadeh, M.; Lu, Z.; Liu, Z.; Gándara, F.; Furukawa, H.; Wan, S.; Augustyn, V.; Chang, R.; Liao, L.; Zhou, F.; Perre, E.; Ozolins, V.; Suenaga, K.; Duan, X.; Dunn, B.; Yamamto, Y.; Terasaki, O.; Yaghi, O. M. New Porous Crystals of Extended Metal-Catecholates. *Chem. Mater.* **2012**, *24*, 3511–3513.

(16) Huang, X.; Li, H.; Tu, Z.; Liu, L.; Wu, X.; Chen, J.; Liang, Y.; Zou, Y.; Yi, Y.; Sun, J.; Xu, W.; Zhu, D. Highly Conducting Neutral Coordination Polymer with Infinite Two-Dimensional Silver-Sulfur Networks. *J. Am. Chem. Soc.* **2018**, *140*, 15153–15156.

(17) Huang, X.; Sheng, P.; Tu, Z.; Zhang, F.; Wang, J.; Geng, H.; Zou, Y.; Di, C. A.; Yi, Y.; Sun, Y.; Xu, W.; Zhu, D. A Two-Dimensional p-d Conjugated Coordination Polymer with Extremely High Electrical Conductivity and Ambipolar Transport Behaviour. *Nat. Commun.* **2015**, *6*, 7408.

(18) Kambe, T.; Sakamoto, R.; Hoshiko, K.; Takada, K.; Miyachi, M.; Ryu, J. H.; Sasaki, S.; Kim, J.; Nakazato, K.; Takata, M.; Nishihara, H. p-Conjugated Nickel bis(dithiolene) Complex Nanosheet. *J. Am. Chem. Soc.* **2013**, *135*, 2462–2465.

(19) Lahiri, N.; Lotfizadeh, N.; Tsuchikawa, R.; Deshpande, V. V.; Louie, J. Hexaaminobenzene as a Building Block for a Family of 2D Coordination Polymers. *J. Am. Chem. Soc.* **2017**, *139*, 19–22.

(20) Sheberla, D.; Bachman, J. C.; Elias, J. S.; Sun, C. J.; Shao-Horn, Y.; Dincă, M. Conductive MOF Electrodes for Stable Supercapacitors with High Areal Capacitance. *Nat. Mater.* **2017**, *16*, 220–224.

(21) Sheberla, D.; Sun, L.; Blood-Forsythe, M. A.; Er, S.; Wade, C. R.; Brozek, C. K.; Aspuru-Guzik, A.; Dincă, M. High Electrical

DOI: 10.1021/jacs.9b08601
J. Am. Chem. Soc. 2019, 141, 16884–16893

Conductivity in Ni_3(2,3,6,7,10,11-hexaiminotriphenylene)$_2$, a Semiconducting Metal-Organic Graphene Analogue. *J. Am. Chem. Soc.* **2014**, *136*, 8859−8862.
(22) Park, J.; Hinckley, A. C.; Huang, Z.; Feng, D.; Yakovenko, A. A.; Lee, M.; Chen, S.; Zou, X.; Bao, Z. Synthetic Routes for a 2D Semiconductive Copper Hexahydroxybenzene Metal-Organic Framework. *J. Am. Chem. Soc.* **2018**, *140*, 14533−14537.
(23) DeGayner, J. A.; Jeon, I. R.; Sun, L.; Dincă, M.; Harris, T. D. 2D Conductive Iron-Quinoid Magnets Ordering up to T_c = 105 K via Heterogenous Redox Chemistry. *J. Am. Chem. Soc.* **2017**, *139*, 4175−4184.
(24) Aubrey, M. L.; Wiers, B. M.; Andrews, S. C.; Sakurai, T.; Reyes-Lillo, S. E.; Hamed, S. M.; Yu, C. J.; Darago, L. E.; Mason, J. A.; Baeg, J. O.; Grandjean, F.; Long, G. J.; Seki, S.; Neaton, J. B.; Yang, P.; Long, J. R. Electron Delocalization and Charge Mobility as a Function of Reduction in a Metal-Organic Framework. *Nat. Mater.* **2018**, *17*, 625−632.
(25) Cutler, A. R.; Dolphin, D. A Mechanistic Study of Metal Template Syntheses of Dibenzo-tetraaza(14)annulene Macrocyclic Complexes. *J. Coord. Chem.* **1976**, *6*, 59−61.
(26) Weiss, M. C.; Gordon, G.; Goedken, V. L. Crystal and Molecular Structure of the Macrocyclic Nickel(II) Complex [Ni-($C_{18}H_{14}N4$)]: Dibenzo[b,i][1,4,8,11]tetraaza[14]annulenenickel(II). *Inorg. Chem.* **1977**, *16*, 305−310.
(27) Mountford, P. Dibenzotetraaza[14]annulenes: Versatile Ligands for Transition and Main Group Metal Chemistry. *Chem. Soc. Rev.* **1998**, *27*, 105−115.
(28) Cotton, F. A.; Czuchajowska, J. Recent Developments in the Chemistry of Mono- and Dinuclear Complexes of the Macrocyclic Dianion, 5,7,12,14-Tetramethyldibenzo[b,i][1,4,8,11] tetraazac. *Polyhedron* **1990**, *9*, 2553−2566.
(29) Whyte, A. M.; Shuku, Y.; Nichol, G. S.; Matsushita, M. M.; Awaga, K.; Robertson, N. Planar Ni(II), Cu(II) and Co(II) Tetraaza[14]annulenes: Structural, Electronic and Magnetic Properties and Aapplication to Field Eeffect Transistors. *J. Mater. Chem.* **2012**, *22*, 17967−17975.
(30) Spellane, P. J.; Interrante, L. V.; Kullnig, R. K.; Tham, F. S. Synthesis and Crystal Structure of [Ni(hMedbtaa)]-[TCNQ]. A mixed-Stack Donor-Acceptor Molecular Solid. *Inorg. Chem.* **1989**, *28*, 1587−1590.
(31) Sustmann, R.; Korth, H. G.; Kobus, D.; Baute, J.; Seiffert, K. H.; Verheggen, E.; Bill, E.; Kirsch, M.; de Groot, H. Fe(III) Complexes of 1,4,8,11-Tetraaza[14]annulenes as Catalase Mimics. *Inorg. Chem.* **2007**, *46*, 11416−11430.
(32) Chirila, A.; Gopal Das, B.; Paul, N. D.; de Bruin, B. Diastereoselective Radical-Type Cyclopropanation of Electron-Deficient Alkenes Mediated by the Highly Active Cobalt(II) Tetramethyltetraaza[14]annulene Catalyst. *ChemCatChem* **2017**, *9*, 1413−1421.
(33) Ramle, A. Q.; Khaledi, H.; Hashim, A. H.; Mingsukang, M. A.; Mohd Arof, A. K.; Ali, H. M.; Basirun, W. J. Indolenine-Dibenzotetraaza [14] Annulene Ni (II) Complexes as Sensitizers for Dye-Sensitized Solar Cells. *Dyes Pigm.* **2019**, *164*, 112−118.
(34) Herebian, D.; Bothe, E.; Neese, F.; Weyhermuller, T.; Wieghardt, K. Molecular and Electronic Structures of Bis-(*o*-Diiminobenzosemiquinonato)metal(II) Complexes (Ni, Pd, Pt), Their Monocations and -Anions, and of Dimeric Dications Containing Weak Metal-Metal Bonds. *J. Am. Chem. Soc.* **2003**, *125*, 9116−9128.
(35) Lin, L.-S.; Marks, T. J.; Kannewurf, C. R.; Lyding, J. W.; McClure, M. S.; Ratajack, M. T.; Whang, T.-C. New Class of Electrically Conductive Metallomacrocycles: Iodine-Doped Dihydrodibenzo[b,i][1,4,8,11]tetra-azacyclotetradecine Complexes. *J. Chem. Soc., Chem. Commun.* **1980**, 954.
(36) Noro, S.; Chang, H. C.; Takenobu, T.; Murayama, Y.; Kanbara, T.; Aoyama, T.; Sassa, T.; Wada, T.; Tanaka, D.; Kitagawa, S.; Iwasa, Y.; Akutagawa, T.; Nakamura, T. Metal-Organic Thin-Film Transistor (MOTFT) Based on a Bis(o-diiminobenzosemiquinonate) Nickel(II) Complex. *J. Am. Chem. Soc.* **2005**, *127*, 10012−10013.
(37) Balch, A. L.; Holm, R. H. Complete Electron-Transfer Series of the [M-N4] Type. *J. Am. Chem. Soc.* **1966**, *88*, 5201−5209.
(38) Chave, P.; Honeybourne, C. L. A Template Synthesis of Metal Complexes of Macrocyclic Ligands. *J. Chem. Soc. D* **1969**, *6*, 279.
(39) Khaledi, H.; Olmstead, M. M.; Mohd Ali, H.; Thomas, N. F. Indolenine Meso-Substituted Dibenzotetraaza[14]annulene and Its Coordination Chemistry toward the Transition Metal Ions Mn(III), Fe(III), Co(II), Ni(II), Cu(II), and Pd(II). *Inorg. Chem.* **2013**, *52*, 1926−1941.
(40) Berrios, C.; Cardenas-Jiron, G. I.; Marco, J. F.; Gutierrez, C.; Ureta-Zanartu, M. S. Theoretical and Spectroscopic Study of Nickel(II) Porphyrin Derivatives. *J. Phys. Chem. A* **2007**, *111*, 2706−2714.
(41) Xu, J.; Zhang, W.; Geng, D.; Liu, Y.; Wang, H.; Tang, N.; Yu, G. Magnetic Properties of a Bottom-Up Synthesis Analogous Graphene with N-Doped Zigzag Edges. *Adv. Electron. Mater.* **2015**, *1*, 1500084.
(42) Hoffman, B. M.; Ibers, J. A. Porphyrinic Molecular Metals. *Acc. Chem. Res.* **1983**, *16*, 15−21.
(43) Hunziker, M.; Hilti, B.; Rihs, G. Metallic Conductivity in Metal Tetraaza [14]Annulene Iodides: The Crystal Structures of Dihydrodibenzo-[b,i]-1, 4, 8, 11-tetraazacyclotetradecinenickel and -palladium Iodides. *Helv. Chim. Acta* **1981**, *64*, 82−89.
(44) Kakazai, B. J. A.; Melson, G. A. Aromatic Diamine Complexes. I. Nickel(II) Complexes with o-Phenylenediamine, 1,8-Diaminonaphthalene and 2−2-Diaminobiphenyl. *Inorg. Chim. Acta* **1968**, *2*, 186−190.
(45) Lantos, J.; Szarvas, P.; Gergely, L.; Kedves, F. J.; Czellr, S. Temperature Dependence of the Magnetic Susceptibility of Benzene-1,2-Diamine-Nickel(II) and -Copper(II) Complexes. *Z. Anorg. Allg. Chem.* **1975**, *415*, 169−174.
(46) Martinsen, J.; Pace, L. J.; Phillips, T. E.; Hoffman, B. M.; Ibers, J. A. (Tetrabenzoporphyrinato)nickel(II) Iodide. A Doubly Mixed Valence Molecular Conductor. *J. Am. Chem. Soc.* **1982**, *104*, 83−91.
(47) Wudl, F.; Bryce, M. R. Apparatus for Two-Probe Conductivity Measurements on Compressed Powders. *J. Chem. Educ.* **1990**, *67*, 717−718.
(48) Wang, Y.; Luo, X.; Tseng, L.-T.; Ao, Z.; Li, T.; Xing, G.; Bao, N.; Suzukiis, K.; Ding, J.; Li, S.; Yi, J. Ferromagnetism and Crossover of Positive Magnetoresistance to Negative Magnetoresistance in Na-Doped ZnO. *Chem. Mater.* **2015**, *27*, 1285−1291.
(49) Dou, J. H.; Sun, L.; Ge, Y.; Li, W.; Hendon, C. H.; Li, J.; Gul, S.; Yano, J.; Stach, E. A.; Dincă, M. Signature of Metallic Behavior in the Metal-Organic Frameworks M_3(hexaiminobenzene)$_2$ (M = Ni, Cu). *J. Am. Chem. Soc.* **2017**, *139*, 13608−13611.
(50) Schmidt, M.; Zimmer, F. M.; Magalhaes, S. G. Spin Glass Induced by Infinitesimal Disorder in Geometrically Frustrated Kagome Lattice. *Phys. A* **2015**, *438*, 416−423.
(51) Pati, S. K.; Rao, C. N. Kagome Network Compounds and Their Novel Magnetic Properties. *Chem. Commun.* **2008**, 4683−4693.
(52) Chen, L.; Kim, J.; Ishizuka, T.; Honsho, Y.; Saeki, A.; Seki, S.; Ihee, H.; Jiang, D. Noncovalently Netted, Photoconductive Sheets with Extremely High Carrier Mobility and Conduction Anisotropy from Triphenylene-Fused Metal Trigon Conjugates. *J. Am. Chem. Soc.* **2009**, *131*, 7287−7292.

DOI: 10.1021/jacs.9b08601
J. Am. Chem. Soc. 2019, 141, 16884−16893